Greatly Enhanced Radiative Transfer Enabled by Hyperbolic Phonon Polaritons in α-MoO$_3$

Yikang Chen, Mauricio A. Segovia Pacheco, Hakan Salihoglu, and Xianfan Xu*

Orthorhombic molybdenum trioxide (α-MoO$_3$) is a highly anisotropic hyperbolic material in nature. Within its wide Reststrahlen bands, α-MoO$_3$ has hyperboloidal dispersion that supports bulk propagation of high-k phonon polariton modes. These modes can serve as energy transport channels to greatly enhance radiative heat transfer inside the material. In this work, large radiative transfer enabled by phonon polaritons in α-MoO$_3$ is demonstrated. The study first determines the temperature-dependent permittivity of α-MoO$_3$ from polarized Fourier-Transform Infrared (FTIR) spectroscopy measurements and then uses a many-body radiative heat transfer model to predict the equivalent radiative thermal conductivity of hyperbolic phonon polariton. Contribution of radiative transfer to the total thermal transport is experimentally determined from the Time-Domain Thermoreflectance (TDTR) measurements in a temperature range from −100 to 300 °C. It is found that radiative transfer can account for ≈60% of the total thermal transport at a temperature of 300 °C. That is, conductive thermal transport is enhanced by >100% by radiative transfer, or radiation inside α-MoO$_3$ is greater than that of conduction. These additional energy pathways will have important implications in thermal management in new materials and devices.

1. Introduction

Understanding and controlling thermal transport propels advancements in various fields from science to technology. The ongoing miniaturization of devices, along with the recent development and application of 2D materials,[1–4] underscores the increasing significance of nanoscale heat transfer.[5–7] In contrast to conventional materials where heat is carried by electrons and phonons,[8,9] there is a growing interest in another carrier, phonon polariton, which offers promising prospects for efficient heat dissipation in compact devices and integrated circuits.[10–13]

Y. Chen, M. A. S. Pacheco, H. Salihoglu, X. Xu
School of Mechanical Engineering and Birck Nanotechnology Center
Purdue University
West Lafayette, IN 47907, USA
E-mail: xxu@ecn.purdue.edu

Phonon polaritons are electromagnetic waves generated from the coupling of photons and optical phonons.[14–16] Surface phonon polaritons (SPhPs) attract much attention because of the long propagation length in thin films and the possibility of using such phenomena for developing photonic devices.[17,18] For thermal transport, much work has been conducted to demonstrate the unique radiative transfer behavior induced by surface phonon polaritons, in both near field[19–22] and far field.[23–25] For thermal transport along a surface, theoretical works predicted that the heat transport can be enhanced by SPhPs.[10,12,26] Recent experimental works also investigated the contribution of SPhPs to thermal transport.[11,27,28] Notably, it was found that the presence of SPhPs boosts the thermal conductivity of 3C-SiC nanowires by 20% at 300 K when both ends of nanowires are coated by gold.[29] However, there are few studies about radiative heat transport of phonon polariton inside materials, which would require bulk phonon polariton instead of SPhPs.

Hyperbolic phonon polaritons (HPhPs) in hyperbolic materials (HMs) are a type of bulk phonon polariton propagating with large wavevectors inside the material, within the Reststrahlen (RS) frequency bands due to the open hyperboloidal isofrequency k-space contours,[30–32] potentially enhancing the radiative heat transport inside HMs. It has been shown theoretically that radiative heat transfer in HMs could be significantly enhanced (at least 6 orders of magnitude larger than that of blackbody).[33,34] Moreover, a recent experimental study demonstrated that in h-BN, HPhPs contribute up to 27% of the total thermal transfer at 600 K.[35] Compared to h-BN, α-MoO$_3$ is another anisotropic HM which has a much wider range of RS band from 545 to 1006 cm^{-1},[36] comparing to those of h-BN from 760 to 825 cm^{-1} and 1364 to 1614 cm^{-1}.[35] Wider RS bands support more HPhPs to carry thermal energy, which implies that radiative heat transport in α-MoO$_3$ can contribute more to the total thermal transport than that in h-BN. Up to now, several research studies have been conducted to investigate and manipulate HPhPs inside α-MoO$_3$,[37–40] however, no studies on thermal radiation by HPhPs inside α-MoO$_3$ has been reported.

In this work, we demonstrate greatly enhanced radiative transfer by HPhP in α-MoO$_3$ through both theoretical analysis and experimental measurement, that radiative heat transfer contributes

**ADVANCED
SCIENCE NEWS**

www.advancedsciencenews.com

**ADVANCED
FUNCTIONAL
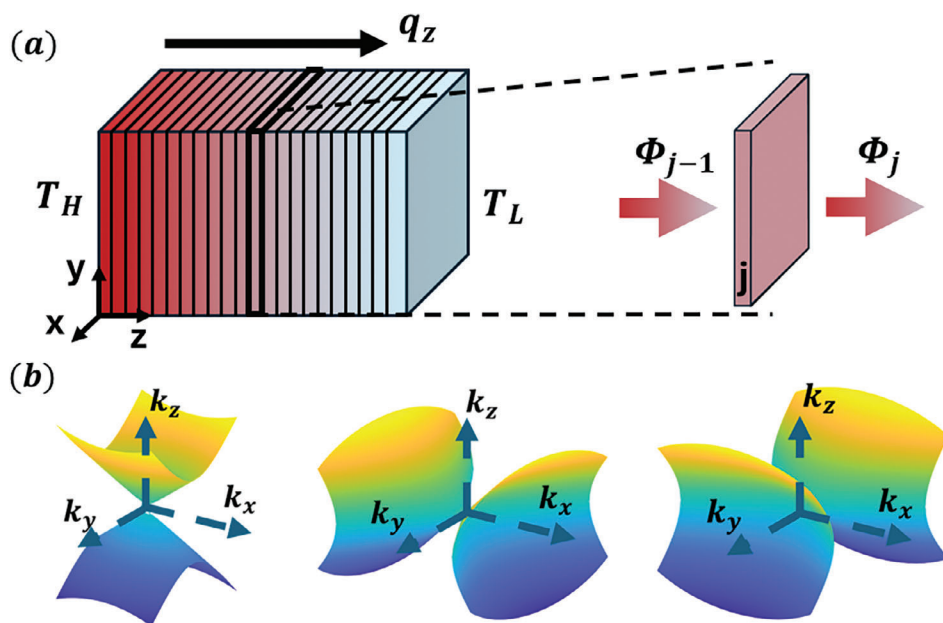MATERIALS**

www.afm-journal.de

Figure 1. Many-body radiative transport model. a) Schematic of the system with a close-up of the heat flux throughout one slab. b) Hyperbolic iso-frequency contours at the Reststrahlen bands of ϵ_z, ϵ_x, and ϵ_y, respectively, from left to right.

more to thermal transport than phonon conduction. A biaxial many-body radiative transport model is first developed to compute phonon polariton heat transfer in α-MoO$_3$ based on an earlier model for uniaxial material using the fluctuation dissipation theorem and Green's function.[35] Experimentally, the permittivity of α-MoO$_3$ is determined by temperature-dependent polarized FTIR measurements fitted to a Lorentz model. The total thermal transfer in the out-of-plane direction, which includes contributions from both phonon and hyperbolic phonon polariton, is measured in a wide range of temperature using TDTR. The significant radiative heat transfer inside the material, greater than that of phonon conduction, indicates this new heat transfer mechanism offers an effective heat dissipation channel in 2D materials.

2. Results and Discussion

Figure 1a shows the schematic of the many-body model where the sliced biaxial HM is sandwiched between hot and cold heat baths at T_H and T_L, respectively. The HM is assumed to be infinite in the in-plane directions (x,y) with uniform temperature for each slab, but experiences temperature variation along the out-of-plane direction (z). Each slab, j, is at a local equilibrium temperature, T_j, which enables the use of the fluctuation-dissipation theorem that relates material temperature with the correlation of source fluctuations in a slab j. This model is continuous and therefore there is no gap between slabs. A previous study developed such a model for the uniaxial HM, h-BN.[35] Here, this model is further developed and extended to biaxial materials for α-MoO$_3$. The net radiative tranfer for a slab, Φ^j, is expressed as:

$$\Phi^j = \Phi_{j-1} - \Phi_j = \int_0^\infty \frac{d\omega}{2\pi} \int_0^{k_{x,m}} \int_0^{k_{y,m}} \frac{dk_x}{\pi} \frac{dk_y}{\pi} \sum_{l \neq j}^N \hbar\omega n_{l,j} \mathcal{T}^{l,j} \tag{1}$$

where ω is frequency of a mode and $\hbar$ is reduced Planck's constant. Φ_j is the radiative thermal energy flux at the boundary between slabs j and $j+1$. $n_{l,j} = 1/(e^{(\frac{\hbar\omega}{k_B T_l})} - 1) - 1/(e^{(\frac{\hbar\omega}{k_B T_j})} - 1)$ is the difference of finding a state occupied by a mode generated at the temperature of slab l, T_l, and slab j, T_j. Summation over l adds up all radiative contribution arising from the interaction of slab j with all other slabs in the N-body system. $\mathcal{T}^{l,j}$ is the energy exchange function (always ≤ 1) which describes how much radiative heat flux can be transferred from slab j to slab l by a mode represented by k_z. The iso-freqency dispersion countors are shown in Figure 1b for the three RS bands in this biaxial material. For the computation, the in-plane anisotropy in the dielectric response requires separate integrations over k_x and k_y. Also, this anisotropy defines the hyperbolic dispersion in the $k_x - k_y$ plane, constraining the range of supported modes. (See Section S1, Supporting Information for the details of implementation of the biaxial many-body model). The upper limits for k_x and k_y are determined by the corresponding lattice constants as π/a or π/b, where a (= 0.396 nm) and b (= 0.370 nm) are the lattice constants of α-MoO$_3$ along the x and y axes, respectively.[41] The thickness for each slab used is chosen to be 0.65 nm after a convergence study. Equation (1) is solved by iteratively varying the temperature of each slab until global thermal equilibrium is reached. Then, the heat flux Φ_j at the interface between the heat bath and the material yields the total radiative heat flux q_z throughout all slabs and an equivalent radiative thermal conductivity k_{rad} is calculated as defined by Fourier's law.

To calculate radiative heat transfer using the many-body model, accurate dielectric constants are required. Polarized and temperature-dependent FTIR measurements are carried out to extract the temperature-dependent dielectric constants. Bulk α-MoO$_3$, acquired from 2D Semiconductors, is exfoliated by tapes to films of several micrometers-thick, and transferred to

**ADVANCED
SCIENCE NEWS**

www.advancedsciencenews.com

**ADVANCED
FUNCTIONAL
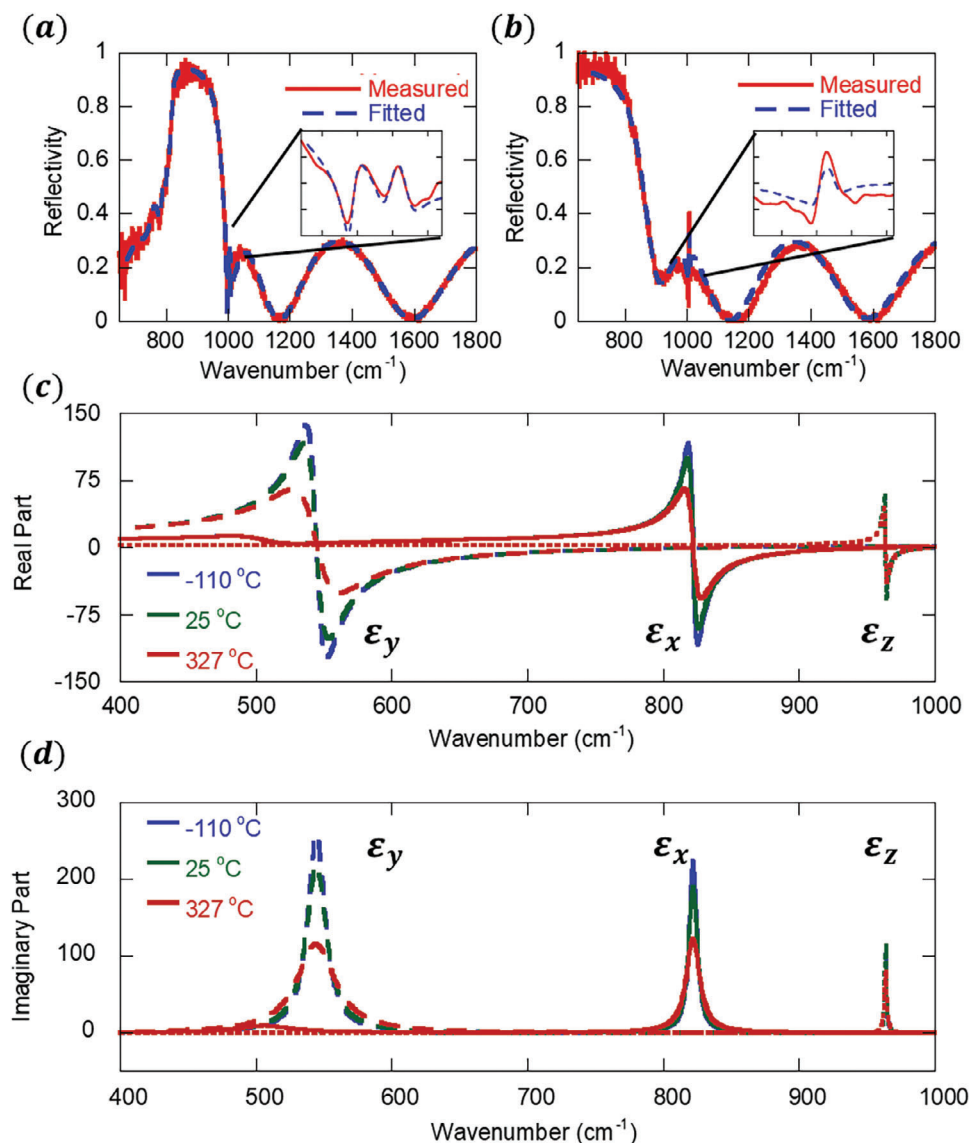MATERIALS**

www.afm-journal.de

Figure 2. Polarization-dependent FTIR reflection spectrum and fitting at 25 °C for a) x-polarized and b) y-polarized reflectivity. A ZnSe polarizer is employed to align the incident polarization direction with the primary in-plane axes. Fitted dielectric constants at -110, 25, and 327 °C. Solid, dashed and dotted lines represent ϵ_x, ϵ_y, and ϵ_z, separately, c) real part of the dielectric constant; d) imaginary part of the dielectric constant. The thickness of α-MoO$_3$ flake used for the FTIR measurement is 4 µm.

a standard silicon wafer. The dielectric constants of α-MoO$_3$ are represented using a multiple-oscillator Lorentz model in which the number of oscillators depends on the number of RS bands, resulting in three oscillators for ϵ_x (i = 3) and one oscillator for either ϵ_y or ϵ_z in α-MoO$_3$. For a specific principal axis, the Lorentz model is expressed as follows[42]:

$$\varepsilon = \varepsilon^\infty \prod_i \frac{(\omega_i^{LO})^2 - \omega^2 - i\Gamma_i\omega}{(\omega_i^{TO})^2 - \omega^2 - i\Gamma_i\omega} \qquad (2)$$

where ε^∞ is the dielectric constant at high frequency, ω^{LO} and ω^{TO} are the upper and lower limits of RS bands, called longitudinal optical (LO) and transverse optical (TO) frequency, respec-

tively, and Γ represents the damping factor. The temperature-dependent permittivity of all axes is determined by fitting FTIR measured reflectivity to the calculated reflectivity based on the Lorentz model.[43] **Figure 2**a,b show the fitted and measured reflection spectrum for different polarizations at room temperature. Figure 2c,d show the permittivity of α-MoO$_3$ at selected temperatures of -110, 25 and 327 °C, where three major RS bands (ϵ_y, ϵ_{x2} and ϵ_z) are centered at 544, 820, and 964 cm^{-1}, respectively. Damping (Γ) is stronger at higher temperatures, resulting in lower peaks in the dielectric constants. Details of the fitted results are provided in Section S2 (Supporting Information). Additionally, α-MoO$_3$ also exhibits hyperbolic behavior in the far IR/THz spectral range.[44] This far IR/THz band is also included in the calculation. The permittivity in the far IR/THz band used
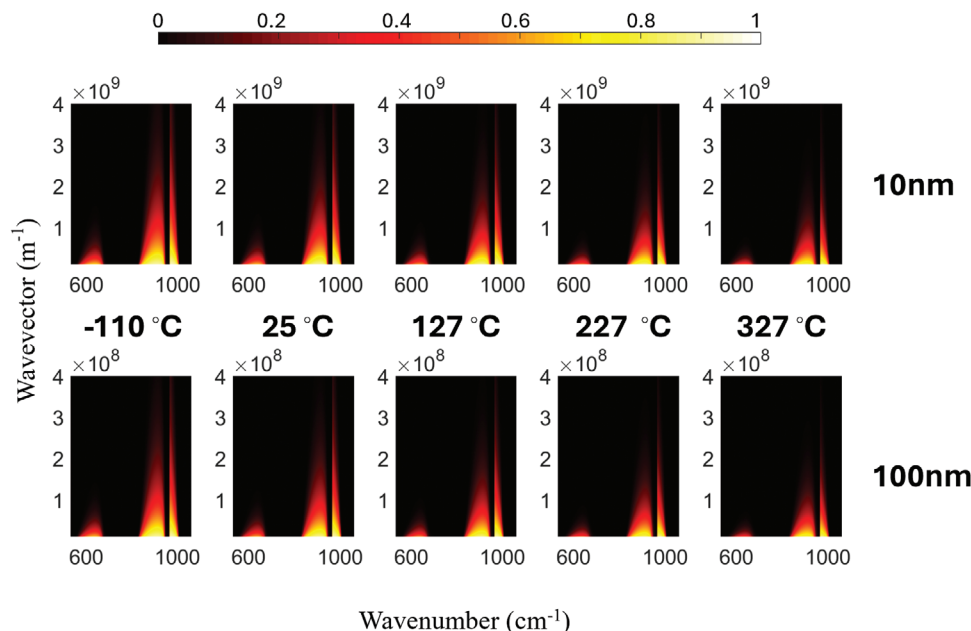
**ADVANCED
SCIENCE NEWS**

www.advancedsciencenews.com

**ADVANCED
FUNCTIONAL
MATERIALS**

www.afm-journal.de

Figure 3. Exchange coefficient $\mathcal{T}^{l,j}$ at different temperatures and over different thicknesses with a fixed wavevector direction ($k_x = k_y$). All subfigures share the same color bar shown on the top. The figures in columns are at temperatures of −110, 25, 127, 227, and 327 °C, respectively, from left to right. The top and bottom rows are for 10 and 100 nm thicknesses, respectively.

in the calculation is discussed in Section S3 (Supporting Information).

Radiative heat transfer in the out-of-plane direction is calculated from the many-body model using the measured temperature-dependent permittivity of α-MoO$_3$. Since hyperbolic phonon-polariton modes are of interest here in analyzing radiative heat transfer, their propagation and decay are analyzed first. **Figure 3** shows the exchange coefficient ($\mathcal{T}^{l,j}$) versus wavenumber and wave vector at a fixed direction ($k_x = k_y$), for thicknesses of 10 nm and 100 nm. The left side of each subplot with wavenumber ranging from 549 to 670 cm^{-1} displays the hyperbolic polariton modes stemming from the RS band of ϵ_y, while the segment with wavenumbers ranging from 824 to 944 cm^{-1} is contributed by the modes from RS bands of ϵ_{x2}. The rightmost segment (965 to 1003 cm^{-1}) originates from the modes from RS bands of ϵ_{x3} (998.9 to 999.4 cm^{-1}) and ϵ_z (963.8 to 1006 cm^{-1}). For all temperatures, the super high-k modes (k >5 × 10^9 m^{-1}) decay fast and their exchange function drops below 5% over a distance of 10 nm, while the modes with one order of magnitude less drops below 5% over a distance of 100 nm. The phonon-polariton modes with k lower than 10^7 m^{-1} have much less loss. It is also seen that the exchange coefficient is a strong function of temperature. Comparing −110 and 327 °C, the exchange function is reduced by roughly 70% for all wavevectors and frequencies. Note that Figure 3 illustrates the exchange function at a specific wavevector direction only. Section S4 (Supporting Information) provides the exchange function along two other directions to illustrate propagation of HPhP along different directions.

Figure 4a shows the spectral irradiance in an α-MoO$_3$ film with a fixed temperature difference of 1 °C between the hot bath and the cold bath. It is seen that hyperbolic phonon polaritons greatly enhance radiation in RS bands, seven to eight orders of

magnitude greater than that of a blackbody. The enhancement in spectral irradiance corresponds to the RS bands of each permittivity. Specifically, the increases in the ranges of 540–820 cm^{-1}, 820–960 cm^{-1}, and 960–1000 cm^{-1} are caused by the RS bands of ϵ_y, ϵ_x, and ϵ_z, respectively. As the thickness of material increases, the energy exchange function $\mathcal{T}^{l,j}$ decreases as discussed in Figure 3. Consequently, the spectral irradiance q_w decreases with thickness.

The total radiation is calculated then converted to a radiative conductivity defined by Fourier's law and is shown in Figure 4b as a function of temperature (blue line). Even though α-MoO$_3$ used in this study has a larger loss at higher temperatures, the calculated $k_{rad,cal}$ increases with temperature, from 0.28 Wm^{-1}K^{-1} at −100 °C to 0.95 Wm^{-1}K^{-1} at 300 °C, because there is higher population of modes at higher temperatures which compensates the loss and leads to an increased $k_{rad,cal}$. However, at higher temperatures, $k_{rad,cal}$ rate of increase is slower because of the larger attenuation of $\mathcal{T}^{l,j}$ from damping.

The total out-of-plane thermal conductivity (k_{tot}) in α-MoO$_3$ is measured using a femtosecond TDTR setup. Details of this system can be found in our previous works[45,46] and are briefly summarized in supplementary information S5 (Supporting Information). The thickness of the film is 3.6 μm. The red solid line in Figure 4b represents the measured k_{tot}, including contribution of both phonon and hyperbolic phonon polaritons, which is found to decrease as the temperature increases.

It is known that for crystalline materials, phonon conductivity varies with temperatures as T^{-1} due to the intrinsic umklapp scattering and saturated heat capacity.[47] 2D materials may behave differently because of the weak van de Waal interactions and the mean free path (MFP) of phonon affected its dimension.[48] Nonetheless, it has been found that α-MoO$_3$ has a maximum

**ADVANCED
SCIENCE NEWS**

www.advancedsciencenews.com

**ADVANCED
FUNCTIONAL
MATERIALS**
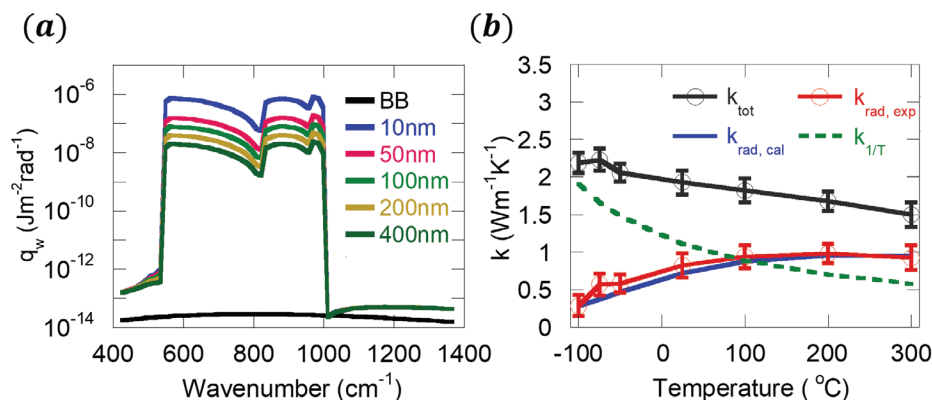
www.afm-journal.de

Figure 4. a) Spectral irradiance comparison between α-MoO$_3$ flakes of various thicknesses (10, 50, 100, 200, 400 nm) and blackbody (BB). b) Temperature-dependent thermal conductivity of k_{tot}, $k_{rad,cal}$, $k_{rad,exp}$ and $k_{T^{-1}}$. The TDTR measurements are conducted at temperatures of −100, −75, −50, 25, 100, 200, and 300 °C, respectively.

out-of-plane MFP of ≈150 nm,[49] significantly smaller than the thickness of the film used in our experiment, implying that the MFP of phonon transport in our α-MoO$_3$ flakes is primarily governed by phonon-phonon scattering and follows a T^{-1} behavior. A recent first-principles calculation, incorporating 3- and 4- phonon scattering, shows bulk α-MoO$_3$ has a $T^{-1.1}$ temperature dependency in the out-of-plane direction over the temperature range from 200 to 1000 K.[50] In Figure 4b, the temperature-dependent phonon contribution in α-MoO$_3$, $k_{T^{-1}}$, is plotted, using the T^{-1} temperature dependency. That is, from −100 °C, where the radiative heat transfer is small (calculated to be 0.28 Wm^{-1}K^{-1}), a T^{-1} decay curve (after subtracting the small radiative contribution) is plotted as is attributed to the phonon conduction. The difference between the measured total thermal conductivity k_{tot} and $k_{T^{-1}}$ is attributed as the contribution from radiation $k_{rad,exp}$. One reason that separating phonon conduction from radiation contribution is possible is that the temperature distribution caused by radiation is almost linear, as shown in Section S6 (Supporting Information). As shown in Figure 4b, $k_{rad,exp}$ and $k_{rad,cal}$ exhibit a similar temperature-dependency and have a close agreement in the measured temperature range from −100 to 300 °C. Figure 4b shows that there is a significant contribution of radiation by HPhPs, which is greater than the phonon contribution at a temperature above 100 °C. At 300 °C, this radiation accounts for ≈60% of total thermal transport.

3. Conclusion

To summarize, we investigate the radiative heat transfer carried by HPhPs in the Restrahlen bands of α-MoO$_3$. A many-body fluctuation theory model accounting for the biaxial dispersion is developed and used to predict the radiative heat transfer in α-MoO$_3$. The temperature-dependent permittivity of α-MoO$_3$ is extracted from FTIR measurements and then fed into the many-body model to obtain the equivalent radiative thermal conductivity. We measure the temperature-dependent total thermal conductivity of α-MoO$_3$ from −100 to 300 °C, from which the radiative thermal conductivity is experimentally determined. The measured radiative heat transfer accounts for a significant portion, up to ≈60% of the total heat transfer at 300 °C, greater than

the contribution from phonon. This indicates that HPhP is a different and significant heat transfer mechanism inside hyperbolic materials, which can be utilized for many thermal engineering applications.

4. Experimental Section

Sample Preparation: Bulk α-MoO$_3$ materials were purchased from 2D Semiconductors. α-MoO$_3$ flakes of several micrometers were exfoliated with Nitto dicing tape and subsequently transferred to standard silicon wafer. The sample was cleaned with toluene, acetone, and IPA to remove residue of adhesive from taps. AFM (NIST-NT) scans were performed to measure the accurate thickness for each flake and then the samples were sent for gold deposition using e-beam evaporation (roughly 100 nm). After deposition, another AFM scan was performed to precisely determine gold thickness.

Temperature-Dependent Dielectric Properties: Nicolet iS50R FTIR was used with a Continuum Microscope to collect reflection spectra of α-MoO$_3$ flake on silicon wafer. A ZnSe polarizer was employed to change incident polarization direction. Sample was placed on a Linkam THMS720 heating stage to control its temperature. A gold-coated silicon piece was also put in chamber to serve as reference. Argon gas was used to purge the chamber of heating stage for 20 min. After waiting for 30 min to allow for thermal stabilization, spectral reflectivity data, collected by a 15x objective lens, was averaged over 50 scans. Details of fitting parameters are given in Section S2 (Supporting Information).

Thermal Conductivity Measurement: Thermal conductivity was measured with a home-built femotosecond time-domain thermoreflectance (TDTR) setup. The 800 nm, 200 fs light was generated from Coherent Mira 900 assembles. Part of 800 nm light was split by beam splitter and sent to BiBO crystal for generating 400 nm light, which served as pump for TDTR measurement. A double lock-in method was used to extract signal. Pump light was modulated by an EOM at 1.28 MHz and probe light was modulated by a mechanical chopper at 400 Hz. The sample was mounted on a heating stage (Linkam THMS 720) and the chamber was purged by ultra-pure argon gas for 20 min. Before data acquisition, the sample stayed for 40 min for thermal stabilization. The measurements were repeated several times to ensure repeatability. A 3D heat transfer model was used to fit ratio curve obtained from TDTR measurement. More details are given in Section S5 (Supporting Information).

Supporting Information

Supporting Information is available from the Wiley Online Library or from the author.

Conflict of Interest

The authors declare no conflict of interest.

Author Contributions

Y.C. prepared samples; measured FTIR spectrum; performed TDTR measurements; and analyzed data. M.A.S.P. performed TDTR measurements and analyzed data. H.K. built biaxial many-body model. X.X. supervised project. All authors contributed to manuscript preparation.

Data Availability Statement

The data that support the findings of this study are available from the corresponding author upon reasonable request.

[1] E. C. Ahn, *NPJ 2D Mater. Appl.* **2020**, *4*, 17.

[2] N. R. Glavin, R. Rao, V. Varshney, E. Bianco, A. Apte, A. Roy, E. Ringe, P. M. Ajayan, *Adv. Mater.* **2020**, *32*, 1904302.

[3] K. Khan, A. K. Tareen, M. Aslam, R. Wang, Y. Zhang, A. Mahmood, Z. Ouyang, H. Zhang, Z. Guo, *J. Mater. Chem. C Mater.* **2020**, *8*, 387.

[4] Q. Qiu, Z. Huang, Q. Qiu, Z. Huang, *Adv. Mater.* **2021**, *33*, 2008126.

[5] G. Chen, *Nanoscale Energy Transport and Conversion: A Parallel Treatment of Electrons, Molecules, Phonons, and Photons*, Oxford University Press, New York, **2005**.

[6] D. G. Cahill, P. V. Braun, G. Chen, D. R. Clarke, S. Fan, K. E. Goodson, P. Keblinski, W. P. King, G. D. Mahan, A. Majumdar, H. J. Maris, S. R. Phillpot, E. Pop, L. Shi, *Appl. Phys. Rev.* **2014**, *1*, 011305.

[7] Z. M. Zhang, *Nano/Microscale Heat Transfer*, Springer International Publishing, Cham, **2020**.

[8] M. L. Storm, M. L. Stormt, *J. Appl. Phys.* **1951**, *22*, 940.

[9] J. M. Ziman, *Electrons and Phonons: The Theory of Transport Phenomena in Solids*, Oxford University Press, Oxford, **2001**.

[10] J. Ordonez-Miranda, L. Tranchant, B. Kim, Y. Chalopin, T. Antoni, S. Volz, *Phys. Rev. Lett.* **2014**, *112*, 055901.

[11] Y. Wu, J. Ordonez-Miranda, S. Gluchko, R. Anufriev, D. D. S. Meneses, L. Del Campo, S. Volz, M. Nomura, *Sci. Adv.* **2020**, *6*, eabb4461.

[12] K. H. Yun, B. J. Lee, S. H. Lee, *Sci. Rep.* **2022**, *12*, 15477.

[13] J. Minyard, T. E. Beechem, *J. Appl. Phys.* **2023**, *134*, 165102.

[14] S. P. S. Porto, B. Tell, T. C. Damen, *Phys. Rev. Lett.* **1966**, *16*, 450.

[15] J. F. Scott, L. E. Cheesman, S. P. S. Porto, *Phys. Rev.* **1967**, *162*, 834.

[16] G. Borstel, H. J. Falge, *Electromagnetic Surface Modes* (Ed.: A. D. Boardman), John Wiley & Sons, Chichester, **1982**.

[17] J. J. Burke, G. I. Stegeman, T. Tamir, *Phys. Rev. B* **1986**, *33*, 5186.

[18] S. Dai, J. Quan, G. Hu, C. W. Qiu, T. H. Tao, X. Li, A. Alù, *Nano Lett.* **2019**, *19*, 1009.

[19] K. Joulain, J. P. Mulet, F. Marquier, R. Carminati, J. J. Greffet, *Surf. Sci. Rep.* **2005**, *57*, 59.

[20] S. Shen, A. Narayanaswamy, G. Chen, *Nano Lett.* **2009**, *9*, 2909.

[21] B. Song, Y. Ganjeh, S. Sadat, D. Thompson, A. Fiorino, V. Fernández-Hurtado, J. Feist, F. J. Garcia-Vidal, J. C. Cuevas, P. Reddy, E. Meyhofer, *Nat. Nanotechnol.* **2015**, *10*, 253.

[22] H. Salihoglu, W. Nam, L. Traverso, M. Segovia, P. K. Venuthurumilli, W. Liu, Y. Wei, W. Li, X. Xu, *Nano Lett.* **2020**, *20*, 6091.

[23] J. J. Greffet, R. Carminati, K. Joulain, J. P. Mulet, S. Mainguy, Y. Chen, *Nature* **2002**, *416*, 61.

[24] N. Dahan, A. Niv, G. Biener, V. Kleiner, E. Hasman, *Appl. Phys. Lett.* **2005**, *86*, 191102.

[25] A. K. Hafeli, E. Rephaeli, S. Fan, D. G. Cahill, T. E. Tiwald, *J. Appl. Phys.* **2011**, *110*, 043517.

[26] D.-Z. A. Chen, A. Narayanaswamy, G. Chen, *Phys. Rev. B* **2005**, *72*, 155435.

[27] L. Tranchant, S. Hamamura, J. Ordonez-Miranda, T. Yabuki, A. Vega-Flick, F. Cervantes-Alvarez, J. J. Alvarado-Gil, S. Volz, K. Miyazaki, *Nano Lett.* **2019**, *19*, 6924.

[28] Y. Wu, J. Ordonez-Miranda, L. Jalabert, S. Tachikawa, R. Anufriev, H. Fujita, S. Volz, M. Nomura, *Appl. Phys. Lett.* **2022**, *121*, 112203.

[29] Z. Pan, G. Lu, X. Li, J. R. McBride, R. Juneja, M. Long, L. Lindsay, J. D. Caldwell, D. Li, *Nature* **2023**, *623*, 307.

[30] Z. Jacob, *Nat. Mater.* **2014**, *13*, 1081.

[31] S. Dai, Z. Fei, Q. Ma, A. S. Rodin, M. Wagner, A. S. McLeod, M. K. Liu, W. Gannett, W. Regan, K. Watanabe, T. Taniguchi, M. Thiemens, G. Dominguez, A. H. Castro Neto, A. Zettl, F. Keilmann, P. Jarillo-Herrero, M. M. Fogler, D. N. Basov, *Science* **2014**, *343*, 1125.

[32] E. E. Narimanov, A. V. Kildishev, *Nat. Photonics* **2015**, *9*, 214.

[33] J. Liu, E. Narimanov, *Phys. Rev. B* **2015**, *91*, 041403.

[34] S. A. Biehs, S. Lang, A. Y. Petrov, M. Eich, P. Ben-Abdallah, *Phys. Rev. Lett.* **2015**, *115*, 174301.

[35] H. Salihoglu, V. Iyer, T. Taniguchi, K. Watanabe, P. D. Ye, X. Xu, *Adv. Funct. Mater.* **2020**, *30*, 1905830.

[36] G. Álvarez-Pérez, T. G. Folland, I. Errea, J. Taboada-Gutiérrez, J. Duan, J. Martín-Sánchez, A. I. F. Tresguerres-Mata, J. R. Matson, A. Bylinkin, M. He, W. Ma, Q. Bao, J. I. Martín, J. D. Caldwell, A. Y. Nikitin, P. Alonso-González, *Adv. Mater.* **2020**, *32*, 1908176.

[37] G. Hu, Q. Ou, G. Si, Y. Wu, J. Wu, Z. Dai, A. Krasnok, Y. Mazor, Q. Zhang, Q. Bao, C.-W. Qiu, A. Alù, *Nature* **2020**, *582*, 209.

[38] G. Álvarez-Pérez, A. González-Morán, N. Capote-Robayna, K. V. Voronin, J. Duan, V. S. Volkov, P. Alonso-González, A. Y. Nikitin, *ACS Photonics* **2022**, *9*, 383.

[39] N. A. Aghamiri, G. Hu, A. Fali, Z. Zhang, J. Li, S. Balendhran, S. Walia, S. Sriram, J. H. Edgar, S. Ramanathan, A. Alù, Y. Abate, *Nat. Commun.* **2022**, *13*, 4511.

[40] S. J. Yu, H. Yao, G. Hu, Y. Jiang, X. Zheng, S. Fan, T. F. Heinz, J. A. Fan, *ACS Nano* **2023**, *17*, 23057.

[41] S. Puebla, R. D'Agosta, G. Sanchez-Santolino, R. Frisenda, C. Munuera, A. Castellanos-Gomez, *NPJ 2D Mater. Appl.* **2021**, *5*, 37.

[42] T. G. Folland, L. Nordin, D. Wasserman, J. D. Caldwell, *J. Appl. Phys.* **2019**, *125*, 191102.

[43] Z. Zheng, N. Xu, S. L. Oscurato, M. Tamagnone, F. Sun, Y. Jiang, Y. Ke, J. Chen, W. Huang, W. L. Wilson, A. Ambrosio, S. Deng, H. Chen, *Sci. Adv.* **2019**, *5*, eaav8690.

[44] T. V. A. G. de Oliveira, T. Nörenberg, G. Álvarez-Pérez, L. Wehmeier, J. Taboada-Gutiérrez, M. Obst, F. Hempel, E. J. H. Lee, J. M. Klopf, I. Errea, A. Y. Nikitin, S. C. Kehr, P. Alonso-González, L. M. Eng, *Adv. Mater.* **2021**, *33*, 2005777.

[45] S. Huang, M. Segovia, X. Yang, Y. R. Koh, Y. Wang, P. D. Ye, W. Wu, A. Shakouri, X. Ruan, X. Xu, *2D Mater.* **2020**, *7*, 015008.

[46] J. Noh, P. R. Chowdhury, M. Segovia, S. Alajlouni, M. Si, A. R. Charnas, S. Huang, K. Maize, A. Shakouri, X. Xu, X. Ruan, P. D. Ye, *IEEE Trans. Electron Devices* **2022**, *69*, 1186.

[47] C. Kittel, *Introduction to Solid State Physics*, 8th ed., John Wiley & Sons, Hoboken, **2005**.

[48] C. Yu, Y. Ouyang, J. Chen, *J. Appl. Phys.* **2021**, *130*, 010902.

[49] A. G. Gokhale, A. Jain, *Appl. Phys. Lett.* **2023**, *123*, 232202.

[50] Z. Tong, T. Dumitrică, T. Frauenheim, *Nano Lett.* **2021**, *21*, 4351.